Symmetry Dictated Grain Boundary State in a Two-Dimensional Topological Insulator

Hyo Won Kim,*,○ Seoung-Hun Kang,○ Hyun-Jung Kim,○ Kisung Chae, Suyeon Cho, Wonhee Ko, Sangjun Jeon, Se Hwang Kang, Heejun Yang, Sung Wng Kim, Seongjun Park, Sungwoo Hwang, Young-Kyun Kwon, and Young-Woo Son*

Read Online

ACCESS | Metrics & More | Article Recommendations | SI Supporting Information

ABSTRACT: Grain boundaries (GBs) are ubiquitous in solids and have been of central importance in understanding the nature of polycrystals. In addition to their classical roles, topological insulators (TIs) offer a chance to realize GBs hosting distinct topological states that can be controlled by their crystal symmetries. However, such roles of crystalline symmetry in two-dimensional (2D) TIs have not been definitively measured yet. Here, we present the first direct evidence of a symmetry-enforced metallic state along a GB in 1T′-MoTe$_2$, a prototypical 2D TI. Using scanning tunneling microscopy, we show a metallic state along a GB with nonsymmorphic lattice symmetry and its absence along another boundary with symmorphic symmetry. Our atomistic simulations demonstrate in-gap Weyl semimetallic states for the former, whereas they demonstrate gapped states for the latter, explaining our observation well. The observed metallic state, tightly linked to its crystal symmetry, can be used to create a stable conducting nanowire inside TIs.

KEYWORDS: Grain boundary, topological insulator, nonsymmorphic symmetry, Weyl semimetallic states, scanning tunneling microscopy, density functional theory calculations
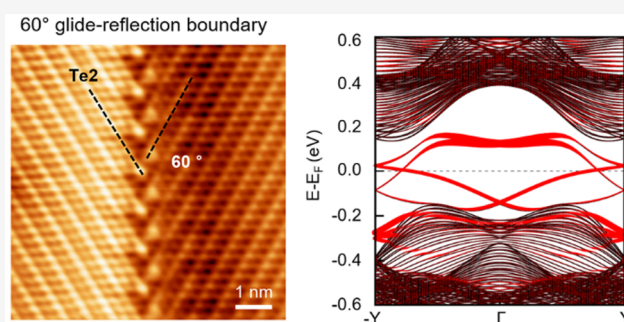
Structural imperfections such as grain boundaries (GBs) and dislocations are important large scale structural defects in studying the nature of polycrystals.[1] Besides their classical roles in determining structural and electronic properties of solids,[1] nowadays, various interesting topological states along the GBs or dislocations can be realized inside topological insulators (TIs).[2−9] Although dislocations inside three-dimensional TIs[5−7,10] are one of the prime candidates to look for, their direct detection and characterization are challenging. In two-dimensional (2D) TIs, their creations and measurements are easier, and moreover, topological states at the GBs or dislocations are intimately related to their lattice symmetry,[6,7] thus providing a quintessential playground to study the relationship between topological electronic structures and crystalline symmetries inside TIs.

Among many 2D materials, various GBs with distinct spatial symmetries can be realized in a 2D transition-metal dichalcogenide, 1T′-MoTe$_2$, thanks to its unusual crystal structure. Because the 1T′ phase of MoTe$_2$ can be understood as a static lattice distortion from its more symmetric but unstable 1T phase,[11] it is possible to create disparate structural phase boundaries between crystalline domains with different orientations while growing the 1T′ structure (hereafter we omit 1T′ for convenience).

Our study of one-dimensional (1D) topological metallic states along GBs of MoTe$_2$ was based on scanning tunneling microscopy (STM) and spectroscopy (STS). In as-grown MoTe$_2$ sample surfaces, we observed an unprecedented GB structure satisfying a nonsymmorphic glide-reflection symmetry and a topological metallic state associated with it. In contrast to this, we could distinguish a semiconducting boundary state along another boundary with a symmorphic mirror symmetry. Our measurement of the existence of topological states depending on the symmetries of GBs was further confirmed by large scale atomistic simulations. We perform multiscale numerical simulations that can compute electronic structures of large structures by obtaining reliable tight-binding parameters for GBs from first-principles computations. Our atomistic simulations show that the Weyl semimetallic Fermionic states exist inside a gap of MoTe$_2$ for a
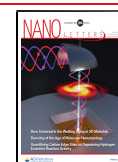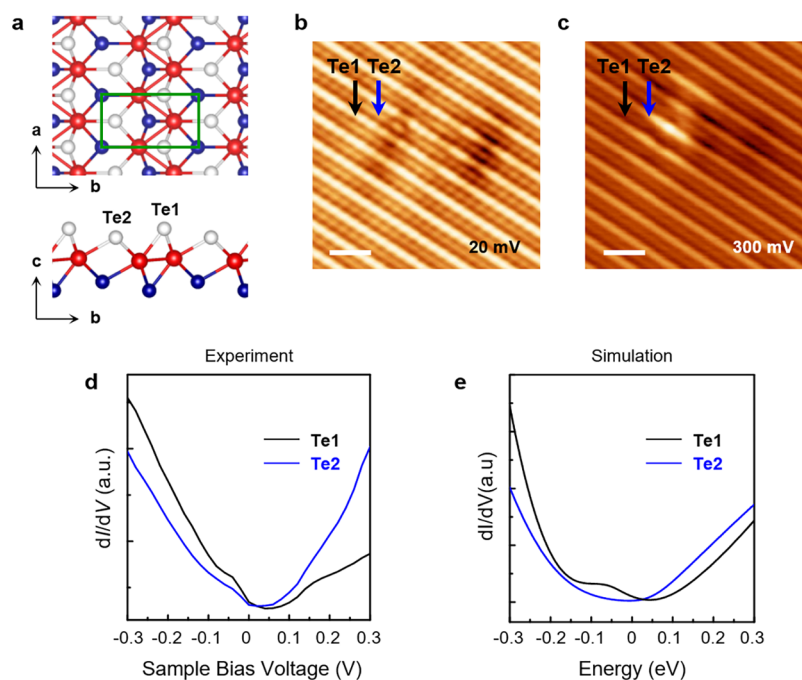
Figure 1. Morphology and electronic structure of a 1T'-MoTe$_2$. (a) Schematic illustration of 1T'-MoTe$_2$. The green box represents a 1T'-MoTe unit cell containing Te1 and Te2 with a height difference relative to the transition-metal plane. (b, c) STM topograph of the 1T'-MoTe$_2$ surface near a defect at $V_s = 20$ mV and $V_s = 300$ mV, respectively ($I_t = 0.5$ nA). Scale bars are 1 nm. The contrast between Te1 and Te2 in the STM image depends on the applied voltages. (d, e) Experimentally obtained (set-point conditions: $V_{set} = 0.025$ V, $I_{set} = 0.1$ nA, $V_{mod} = 10$ mV) and DFT-calculated dI/dV spectra at Te rows, Te1 (black line) and Te2 (blue line), respectively.

GB with a nonsymmorphic symmetry while a gapped spectrum exists for a GB with a symmorphic one, explaining the experimental findings very well.

We first identify the topological nature of the surface layer of an as-grown MoTe$_2$ bulk sample. Although we measured tunneling spectra on the surface of the bulk sample, our measurements clearly indicate that the topmost layer behaves as a single layer detached from the rest of the sample. Such a behavior has already been observed in a similar material[12] as well as in other layered crystals, e.g., graphene-like behavior of the topmost layer of graphite.[13] Our simulated STM images and STSs also support the single-layer-like behavior of the topmost layer of the bulk MoTe$_2$ sample. The simulated images of the single-layer MoTe$_2$ with varying applied voltage also agree with our observations well (see Figure S1 in the Supporting Information). Thanks to effective isolation, we were able to measure the topologically protected metallic state along the truncated step edge by its dI/dV spectra (Figure S2), and the STM images agree well with previous studies.[14,15] In our sample with GBs, in fact, the lattice mismatch between the topmost layer and the others inevitably occurs in one side or both sides of the domain at GBs. In the case of the 60° glide-reflection boundary, the left side of the domain is higher than the right side by 0.08 nm, which is approximately 10% bigger than the ordinary lattice spacing between layers (Figure S3). This nonflat height profile away from GB is observed in every GB including 120° mirror GBs, and our DFT calculation also displays the increased space between the topmost layer and the rest of the layers due to the interlayer stacking configuration. This supports the reduced interlayer coupling strength (see details in Figure S4 in the Supporting Information). We also note here and will discuss later that the distinct topological properties of GBs related with their crystal symmetries are

indeed intact regardless of nature of the remaining bulk underneath the first layer.

In MoTe$_2$, the chalcogen atoms (Te atoms) form quasi-one-dimensional parallel chains where adjacent chains (denoted as rows Te1 and Te2, respectively) have alternative height variations with respect to the transition-metal plane as shown in Figure 1a. The inequivalent rows of Te atoms will play an important role in determining the local crystalline symmetry along GBs later. Te1 and Te2 exhibit different contrast in our STM images. We found that this contrast difference between the two chains also depends on the applied bias voltages; for example, the contrast at 300 mV is reversed in Figure 1c compared to that at 20 mV in Figure 1b (a defect is used as a marker to identify Te1 and Te2 rows in Figure 1b and c) (see details in Figure S5 in the Supporting Information). To figure out the effect of the electronic state, we measured the local dI/dV spectra of the Te1 and Te2 rows. To minimize the set-point effect of spectroscopic measurements, we chose the stabilization bias voltage $V = 25$ mV. Agreeing well with the STM images, the values of dI/dV at different rows cross each other at 20 mV in Figure 1d. The different energy levels of Te1 and Te2 p-orbitals from our first-principles simulation explain the alternating contributions from the two chalcogen atoms to determine the crystal structures of MoTe$_2$ precisely (Figure S5).

Having characterized the topmost layer, we now turn to the formation mechanism of GBs. Suppose that a structural phase transition of a matrix from the high symmetry (1T) phase to the low one (1T') through dimerization of adjacent Mo rows occurs at multiple locations. There are six orientation variants, resulting from the 6-fold improper rotational symmetry (see black and gray dotted arrows in Figure 2a). Excluding trivial and high energy structures, the interfaces between two 1T' phase crystals in different orientations can form four
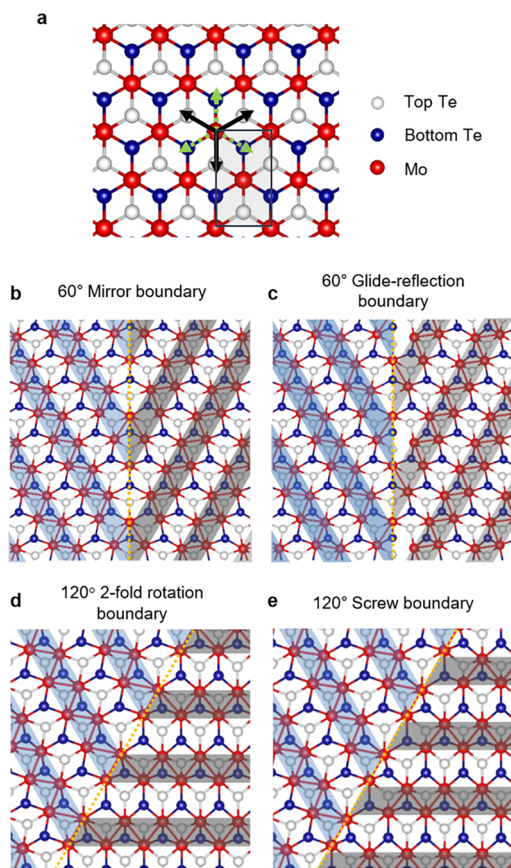
Figure 2. Possible grain boundaries from six orientation variants of 1T′-MoTe$_2$. (a) Three symmetry-equivalent directions (black arrows) of structural distortion in the 1T structure and their opposite three directions (green dotted arrows), which are distinguished by the directions toward top and bottom Te atoms, respectively. The rectangular is a primitive unit cell of the 1T′ phase, which corresponds to the $1 \times \sqrt{3}$ supercell of the 1T phase. (b−e) Possible grain boundary structures determined by the direction of structural distortion with respect to the boundary. To help guide the eyes, dimerized Mo atoms are shaded in blue and black colors.

inequivalent symmetric tilt GBs at angles of either 60° or 120°, which can be categorized by the GB operations that map the right side of the crystal onto the left side. We identified that those GB operations are 60° mirror, 60° glide-reflection, 120° 2-fold rotation, and 120° screw, and the corresponding boundary structures are shown in Figure 2b−e. These low energy GBs were found by a simple GB model considering point group symmetry in addition to coincidence site lattice theory (Figure S6). Furthermore, we found that the 60° glide-reflection and the 120° 2-fold rotation boundaries are the energetically favorable states because their strains are smaller than the others. We confirmed that these two structures match the experimentally observed ones (Figures 3a and 4a) and are approximately 110 meV/formula unit (f.u) and 570 meV/f.u more stable than the 60° mirror and 120° screw GB structures, respectively. We note that the 120° 2-fold rotation boundary was theoretically predicted as a twin boundary induced by strain in single crystalline 1T′-MoTe$_2$,[16] which was also observed experimentally,[17,18] while the 60° glide-reflection boundary has not been reported before.

At the 60° glide-reflection boundary, the STM image in Figure 3a shows its nonsymmorphic symmetry nature clearly.

The bright rows of chalcogen atoms on the right side of the boundary show abrupt discontinuities to those on the left side. The bright rows on the right side can be mapped onto the left ones by simultaneous operations of mirroring and translation by a half-unit translation with respect to the GB. The measured dI/dV spectrum at the boundary, shown in Figure 3b (red line), reveals a peak near −70 mV, whereas the local dI/dV spectrum far away from it (black and blue lines) shows no feature at −70 mV, similarly to the local spectrum of the pristine sample (Figure 1d). We note that the observed spectrum in Figure 3b is similar to recently reported topological edge states in 1T′-WTe$_2$[12,14,15] and our results on the step edge of 1T′-MoTe$_2$ (Figure S2). The peak is spatially localized at the boundary within ∼2 nm width as clearly seen in the spatial dI/dV maps in Figure 3d and Figure S2, respectively.

The spatially and energetically localized one-dimensional metallic state along the GB with nonsymmorphic symmetry is in sharp contrast to states in the other boundary with symmorphic symmetry. Unlike the case of the 60° glide-reflection boundary, the STM image of the 120° 2-fold rotation boundary shows continuous bright rows across the boundary with kinks as shown in Figure 4a. Thus, the right side of the STM image can be mapped onto the left one by a 2-fold rotation operation. Its dI/dV spectrum in Figure 4b also reveals stark differences, i.e., the spectrum measured at the GB denoted by the green line shows the two peaks at −30 and 85 mV and the bulk spectrum by the black line shows the gap of quantum spin Hall state around −70 mV. The spatial distributions of the peaks at 85 and −30 mV in Figure 4d indicate that the states associated with the peaks are broadly distributed along the boundaries and that their intensities are lower than that of the 60° glide-reflection boundary (further dI/dV maps are presented in Figure S7).

Our theoretical simulations of STM images and dI/dV spectra agree with experimental observations quite well. In Figures 3e and 4e, the simulated STM images for the two different GB structures are displayed. The images of the fully relaxed atomic geometries are computed with the constant current condition[19] and show that the patterns of bright rows of chalcogen atoms clearly reflect the underlying crystal symmetries of the GBs. We also simulated the local dI/dV spectra at GBs and away from them as shown in Figures 3f and 4f. The resulting spectra also agree well with our observations, showing a single peak at the energetic position of the bulk gap for the 60° glide-reflection boundary and two split peaks for the 120° 2-fold rotation boundary. Our projected 1D band structures along the momentum parallel to the grain boundary direction (Figures 3g and 4g) show sharp differences between the two GBs. Thus, it is evident that these contrasting features of the band structures are responsible for the different dI/dV spectra for the two disparate GBs.

For the nonsymmorphic case in Figure 3g, the four bands are entangled to form a Weyl semimetallic state, while for the symmorphic case in Figure 4g, the entangled bands are broken to open a gap at the Fermi energy, resulting in two sets of bowtie-shaped bands separated by a gap. Such an interesting difference can be understood in terms of a mutual interaction across the GBs between the edge states of 2D TIs on the both sides of the GBs. Assuming first no interaction across the GBs, there should be topologically protected edge states on the both sides. Now, with turning on interaction, the edge states with the same spin orientation on both sides interact each other and
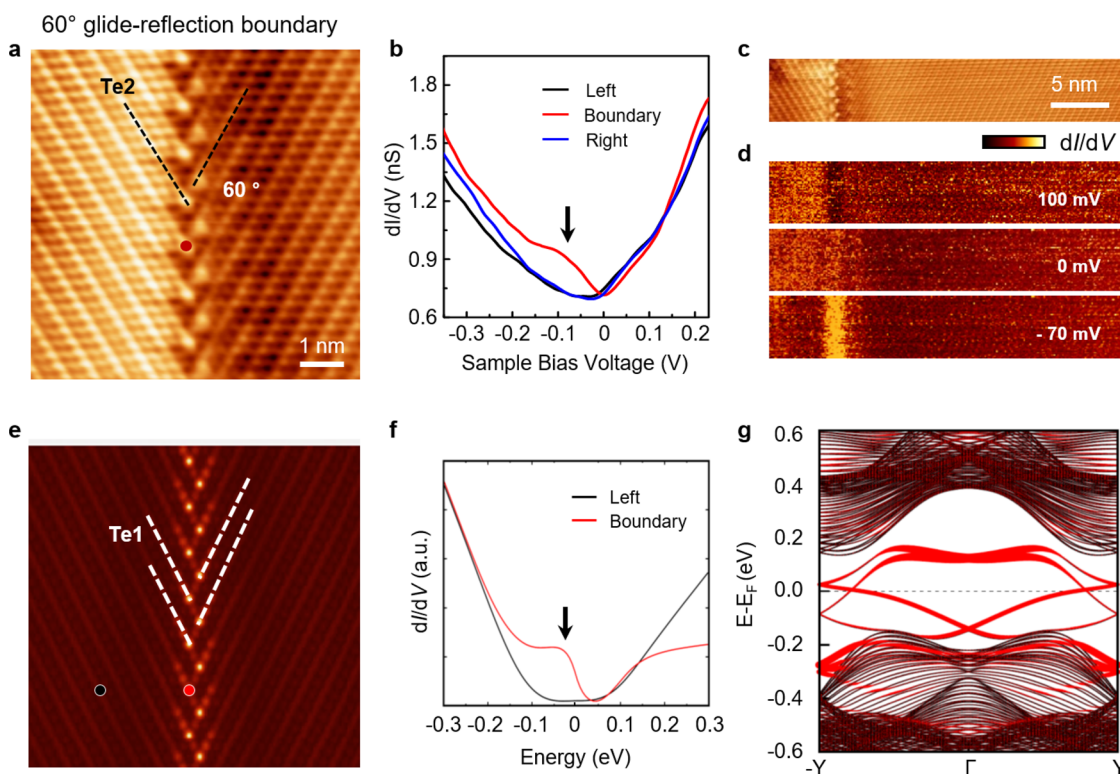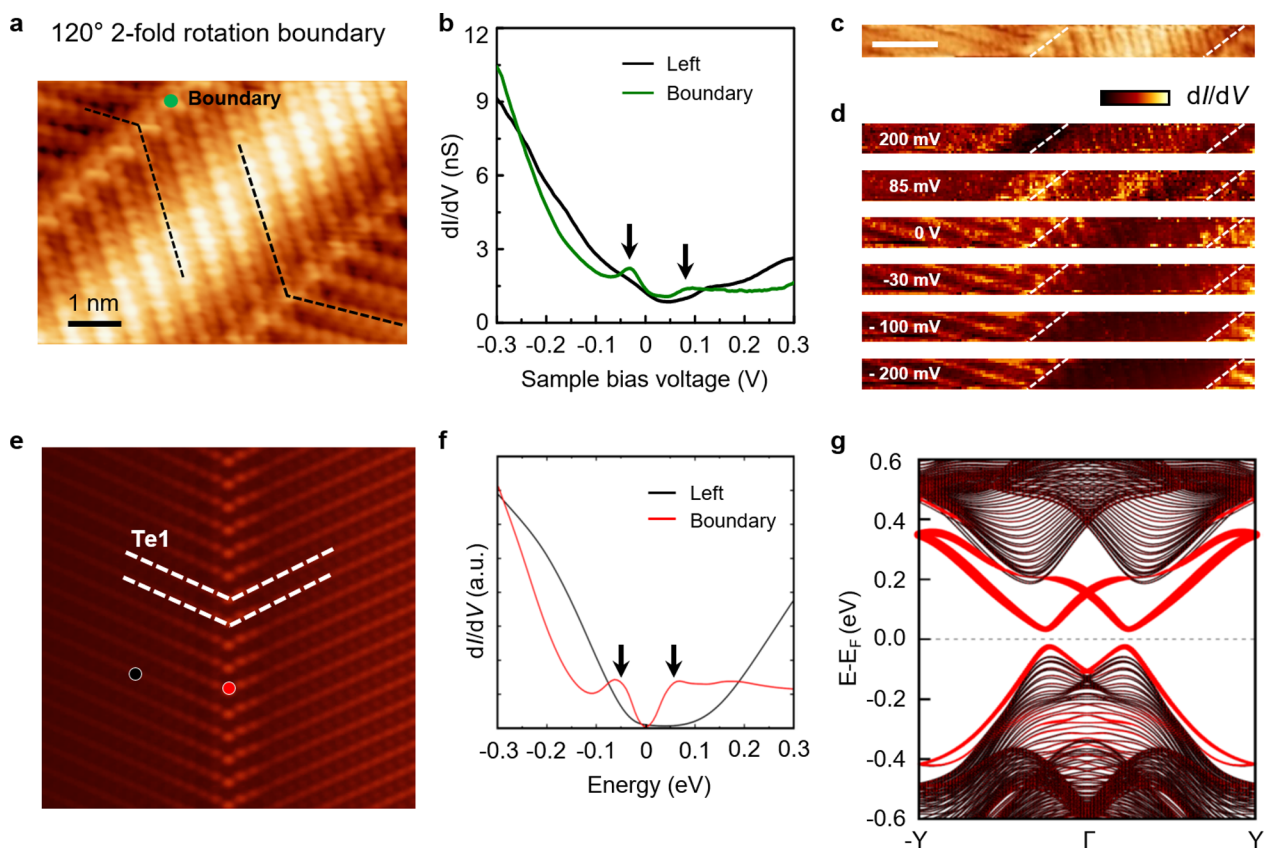
Figure 3. Geometrical and electronic structures of 60° glide-reflection boundaries of 1T′-MoTe$_2$. (a) STM topograph of 60° glide-reflection boundary (V_s = 0.3 V, I = 0.5 nA). (b) Averaged dI/dV spectra taken at left area (black line) and right area (blue line) and dI/dV spectrum obtained at the position indicated by the red dot in (a) (red line) (set-point conditions: V_{set} = 0.5 V, I_{set} = 0.5 nA, V_{mod} = 10 mV). (c) STM topograph. (d) dI/dV maps obtained over the area shown in (c) for bias voltages V = 100, 0, and −70 mV from top to bottom. (e) Simulated STM image of 60° glide-reflection boundary on the V_s = 0.35 V. To match charge neutral points and band widths between experimental dI/dV in Figure 3b and the simulated one in Figure 3f, we simulated STM image within energy window from +100 meV to +450 meV. (f) Simulated dI/dV at the left area (black line) and boundary (red line) denoted by black and red dots in a, respectively. (c) Band structure for the 60° glide-reflection boundary with the twin boundary structure.

their bands open a spectral gap or show avoided crossings wherever they overlap each other. Thanks to the time reversal symmetry, the Kramers pairs still exist at the time reversal invariant momenta (TRIM) points. Under these circumstances, the crystalline symmetry plays an important role. With symmorphic lattice symmetries, all overlapped bands of edge states belong to the different sides of the GB open spectral gaps except TRIM points so that the resulting bands look like the bowtie shape as already discussed in previous studies.[6,7] Moreover, edge states on each side have half-filled bands so that the Fermi energy should locate at the gap between the two bowtie bands, agreeing with our simulation as well as observation in Figure 4.

Now, for the case of nonsymmorphic symmetry, additional quantum numbers for the bands of edge states can be assigned by the nonsymmophic symmetry operator.[20] So, the Kramers pair at one TRIM point should change their partners without avoided band crossing at the next TRIM point, and absence of inversion symmetry opens spectral gaps otherwise, resulting in one-dimensional Weyl semimetallic bands.[20] Like the symmorphic case, the Fermi level should be at the Weyl points,[20] also agreeing with our observation and simulation in Figure 3. Since the nonsymmorphic symmetry along the GB guarantees protected band crossings with linear dispersions at low energy, the spectroscopic signature in Figure 3b and 3f looks quite similar to one (Figure S2) shown at the edge of topological insulating MoTe$_2$.

The quasi-particle interferences (QPIs) acquired along the two GBs also provide further evidence of the critical roles of lattice symmetry (see details in Figure S8). We obtained the distinct QPI from each GB, agreeing well with our QPI simulations. The former case exhibits the enhance interference signal where the Weyl semimetallic exists in the energy gap of the first layer while the latter shows a constant background metallic signal. We emphasize here that the underlying metallic bulk behaves as a constant background in spectroscopic signals because of the effective isolation of the first layer as discussed above and the nearly constant density of states of bulk near the Fermi energy. To confirm this, we simulated effects of metallic underlying layers on nonsymmorphic GB states and found that the metallic substrate indeed does not alter the nature of the GB as shown in Figure S10.

In conclusion, we demonstrate the presence and absence of a metallic grain boundary state with and without the nonsymmorphic lattice symmetry inside a topological insulating TMD material. We confirm that the Weyl semimetallic metallic state along the nonsymmorphic grain boundary shows a spectroscopic signal similar to that from the topological edge states of 2D quantum spin Hall insulators. Considering the typical growth method for TMDs,[21] GBs between crystalline domains with different orientations are inevitable. Thus, our experimental demonstration of protected metallic states here not only provides the first direct evidence of the existence of the symmetry-enforced Weyl metallic state along dislocated atomic defects with distinct crystal symmetry but also

Figure 4. Geometrical and electronic structures of 120° 2-fold rotation boundary. (a) STM topograph of the 120° 2-fold rotation boundary (V_s = 0.3 V, I = 0.1 nA). (b) Averaged dI/dV spectrum taken at left area (black line) and dI/dV spectrum obtained at the position indicated by the white dot in e (green line) (set-point conditions: V_{set} = 0.2 V, I_{set} = 0.3 nA, V_{mod} = 10 mV). (c) STM topograph. Scale bar is 2 nm. (d) dI/dV maps obtained over the area shown in (c) for bias voltages V = 200, 85, 0, −30, −100, and −200 mV from top to bottom. The dashed white lines are used as guides indicating 120° boundaries. (e) Simulated STM image of 120° 2-fold rotation boundary on the V_s = 0.3 V. (f) Simulated dI/dV at the left area (black line) and boundary (red line) denoted by black and red dots in (d), respectively. (f) Band structure for the 120° 2-fold rotation boundary.

represents a possible route to grow the robust metallic nanowires inside the insulator once the growth of the crystalline structure of TMDs can be controlled.

■ **SAMPLE PREPARATION**

High-quality 1T′-MoTe$_2$ single crystals were synthesized using the NaCl-Flux method. A stoichiometric mixture of Mo and Te powders was sintered with sodium chloride (NaCl) at 1373 K for 30 h in evacuated silica tubes. Then, the samples were cooled to 1223 K at a rate of 0.5 K/h, followed by rapid cooling to room temperature by quenching with water. The resulting 1T′-MoTe$_2$ single crystal exhibited a large magnetoresistance and residual resistance ratio, exceeding 32000 and 350, respectively, indicating that Te deficiency is less than 1%.[22]

■ **SCANNING TUNNELING MICROSCOPY/SPECTROSCOPY MEASUREMENTS**

We performed the experiments in a commercial low-temperature STM instrument (UNISOKU Co., Ltd., Osaka, Japan) at 2.8 K. A 1T′-MoTe$_2$ single-crystal sample was cleaved in an ultrahigh vacuum chamber (∼10^{-10} Torr) at room temperature and then transferred to the low-temperature STM sample stage, where the temperature was maintained at 2.8 K. The STS measurements were performed using a standard lock-in technique with a bias modulation of 5 mV at 1 kHz.

■ **DENSITY FUNCTIONAL THEORY AND TIGHT-BINDING CALCULATIONS**

To investigate the structural and electronic properties of 1T′-MoTe$_2$ and its grain boundaries, we performed *ab initio* calculations based on density functional theory (DFT)[23,24] as implemented in the VASP code.[25,26] Projector augmented wave potentials[27,28] were employed to describe the valence electrons, and the electronic wave functions were expanded by a plane wave basis set with the cutoff energy of 450 eV; atomic relaxation was continued until the Hellmann−Feynman force acting on every atom became lower than 0.03 eV/Å. For more precise calculations, we included the dipole correction. The Perdew−Burke−Ernzerhof (PBE) form[29] was employed for the exchange-correlation functional in the generalized gradient approximation (GGA). The Brillouin zone (BZ) was sampled using a 10 × 10 × 1 k-grid for the primitive unit cell of 1T′ MoTe$_2$. The spin−orbit coupling (SOC) effect and on-site Coulomb repulsion (U) were included in all calculations. These parameters have been thoroughly demonstrated to describe the exact characteristic of the single layer 1T′-MoTe$_2$.[30] For the optimization of the GB structures of 1T′-MoTe$_2$, we adopted the basis consisting of pseudoatomic orbitals (PAOs) with a single-ζ basis set, as implemented in the SIESTA code.[31,32] The exchange correlation (XC) functional was treated with GGA as used for VASP. The behavior of valence electrons was described by a norm-conserving

Troullier—Martins pseudopotential[33] with scalar-relativistic effect in the Kleinman—Bylander factorized form,[34] and $4d^5 5s^1 5p^1$ and $5s^2 5p^4$ electrons for molybdenum and tellurium are considered to the valence levels for the pseudopotential. The charge density has been determined self-consistently on a real space mesh with a high cutoff energy of 450 Ry, sufficient for total energy convergence to within 1 meV/atom. The energy shift due to the spatial confinement of the PAO basis functions[35] was limited to less than 0.01 Ry. We used periodic boundary conditions and a periodic array of slabs separated by a vacuum region of $\geq$30 Å throughout the study. The BZ was sampled using $1 \times 5 \times 1$ and $1 \times 3 \times 1$ k-grids for 120° and 60° GBs of 1T' $MoTe_2$, respectively. To investigate the electronic properties of the GBs, we constructed the Slater—Koster type tight-binding (TB) model which successfully reproduces the DFT band structure for the monolayer 1T-$MoTe_2$ near the Fermi level. Here, we assumed five d-orbitals per Mo atom and s- and three p-orbitals per Te atom. Further details of the tight-binding Hamiltonian H in real space are provided in the Supporting Information.

ASSOCIATED CONTENT

⑤ Supporting Information

The Supporting Information is available free of charge at https://pubs.acs.org/doi/10.1021/acs.nanolett.0c01756.

Dependence on the number of layers of 1T'-$MoTe_2$, topologically protected metallic state of 1T'-$MoTe_2$, effect of the lattice mismatch on the topmost layer and the rest of the sample at the boundaries, bias-dependence of STM topographs and dI/dV maps of 1T'-$MoTe_2$, symmetry and formation energy of grain boundaries, differential conductance maps, quasi-particle interference (QPI) acquired along the 60° glide-reflection boundary and 2 nm away from the boundary, DFT-calculated DOS of Te atoms at 120° 2-fold rotation boundary, effects of metallic substrates on GBs, and tight-binding model for 1T'-$MoTe_2$ (PDF)

AUTHOR INFORMATION

Corresponding Authors

Hyo Won Kim — *Samsung Advanced Institute of Technology, Suwon 13595, Korea;* ⓞ orcid.org/0000-0001-8837-1727; Email: hyowon98.kim@samsung.com

Young-Woo Son — *Korea Institute for Advanced Study, Seoul 02455, Korea;* Email: hand@kias.re.kr

Authors

Seoung-Hun Kang — *Korea Institute for Advanced Study, Seoul 02455, Korea*

Hyun-Jung Kim — *Korea Institute for Advanced Study, Seoul 02455, Korea*

Kisung Chae — *Korea Institute for Advanced Study, Seoul 02455, Korea;* ⓞ orcid.org/0000-0003-1628-408X

Suyeon Cho — *Division of Chemical Engineering and Materials Science, Ewha Womans University, Seoul 03760, Korea;* ⓞ orcid.org/0000-0003-1931-9663

Wonhee Ko — *Samsung Advanced Institute of Technology, Suwon 13595, Korea; Center for Nanophase Materials Sciences, Oak Ridge National Laboratory, Oak Ridge, Tennessee 37831, United States*

Sangjun Jeon — *Department of Physics, Chung-ang University, Seoul 06987, Korea;* ⓞ orcid.org/0000-0002-3134-7838

Se Hwang Kang — *Department of Energy Science, Sungkyunkwan University, Suwon 440-746, Korea*

Heejun Yang — *Department of Energy Science, Sungkyunkwan University, Suwon 440-746, Korea;* ⓞ orcid.org/0000-0003-0502-0054

Sung Wng Kim — *Department of Energy Science, Sungkyunkwan University, Suwon 440-746, Korea;* ⓞ orcid.org/0000-0002-4802-5421

Seongjun Park — *Samsung Advanced Institute of Technology, Suwon 13595, Korea*

Sungwoo Hwang — *Samsung Advanced Institute of Technology, Suwon 13595, Korea*

Young-Kyun Kwon — *Korea Institute for Advanced Study, Seoul 02455, Korea; Department of Physics and Research Institute for Basic Sciences, Kyung Hee University, Seoul 02447, Korea;* ⓞ orcid.org/0000-0001-6027-8408

Complete contact information is available at:
https://pubs.acs.org/10.1021/acs.nanolett.0c01756

Author Contributions

ᴼH.W.K., S.-H.K., and H.-J.K. contributed equally to this work. H.W.K. conceived the experiment, and H.W.K. and Y.-W.S. designed and supervised the project. H.W.K. conducted the STM and STS experiments. S.-H.K. and H.-J.K. performed simulations. K.C. carried out grain-boundary structure analysis. S.C., S.H.K., H.Y., and S.W.K. made the samples. H.W.K., W.K., S.J., S.P., S.W.H., Y.K.K., and Y.-W.S. helped to interpret and understand the data. H.W.K. and Y.-W.S. wrote the manuscript with input and comments from all authors.

Notes

The authors declare no competing financial interest.

ACKNOWLEDGMENTS

REFERENCES

(1) Sutton, A. P.; Balluffi, R. W. *Interfaces in Crystalline Materials*; Clarendon Press: 1995.

(2) Kane, C. L.; Mele, E. J. Quantum spin Hall effect in graphene. *Phys. Rev. Lett.* **2005**, *95*, 226801.

(3) Bernevig, B. A.; Hughes, T. L.; Zhang, S.-C. Quantum spin Hall effect and topological phase transition in HgTe quantum wells. *Science* **2006**, *314*, 1757.

(4) König, M.; Wiedmann, S.; Brüne, C.; Roth, A.; Buhmann, H.; Molenkamp, L. W.; Qi, X.-L.; Zhang, S.-C. Quantum spin Hall insulator state in HgTe quantum wells. *Science* **2007**, *318*, 766.

(5) Ran, Y.; Zhang, Y.; Vishwanath, A. One-dimensional topologically protected modes in topological insulators with lattice dislocations. *Nat. Phys.* **2009**, *5*, 298.

(6) Juričić, V.; Mesaros, A.; Slager, R.-J.; Zaanen, J. Universal probes of two-dimensional topological insulators: dislocation and π flux. *Phys. Rev. Lett.* **2012**, *108*, 106403.

(7) Slager, R.-J.; Mesaros, A.; Juričić, V.; Zaanen, J. Interplay between electronic topology and crystal symmetry: Dislocation-line modes in topological band insulators. *Phys. Rev. B: Condens. Matter Mater. Phys.* **2014**, *90*, 241403.

(8) Drozdov, I. K.; Alexandradinata, A.; Jeon, S.; Nadj-Perge, S.; Ji, H.; Cava, R. J.; Andrei Bernevig, B.; Yazdani, A. One-dimensional topological edge states of bismuth bilayers. *Nat. Phys.* **2014**, *10*, 664.

(9) Shi, Y.; Kahn, J.; Niu, B.; Fei, Z.; Sun, B.; Cai, X.; Francisco, B. A.; Wu, D.; Shen, Z.-X.; Xu, X.; Cobden, D. H.; Cui, Y.-T. Imaging quantum spin Hall edges in monolayer WTe_2. *Sci. Adv.* **2019**, *5*, No. eaat8799.

(10) Nayak, A. K.; Reiner, J.; Queiroz, R.; Fu, H.; Shekhar, C.; Yan, B.; Felser, C.; Avraham, N.; Beidenkopf, H. Resolving the topological classification of bismuth with topological defects. *Sci. Adv.* **2019**, *5*, No. eaax6996.

(11) Keum, D. H.; Cho, S.; Kim, J. H.; Choe, D.-H.; Sung, H.-J.; Kan, M.; Kang, H.; Hwang, J.-Y.; Kim, S. W.; Yang, H.; Chang, K. J.; Lee, Y. H. Bandgap opening in few-layered monoclinic $MoTe_2$. *Nat. Phys.* **2015**, *11*, 482.

(12) Peng, L.; Yuan, Y.; Li, G.; Yang, X.; Xian, J.-J.; Yi, C.-J.; Shi, Y.-G.; Fu, Y.-S. Observation of topological states residing at step edges of WTe_2. *Nat. Commun.* **2017**, *8*, 659.

(13) Li, G.; Andrei, E. Y. Observation of Landau levels of Dirac fermions in graphite. *Nat. Phys.* **2007**, *3*, 623.

(14) Jia, Z.-Y.; Song, Y.-H.; Li, X.-B.; Ran, K.; Lu, P.; Zheng, H.-J.; Zhu, X.-Y.; Shi, Z.-Q.; Sun, J.; Wen, J.; Xing, D.; Li, S.-C. Direct visualization of a two-dimensional topological insulator in the single-layer 1T'-WTe_2. *Phys. Rev. B: Condens. Matter Mater. Phys.* **2017**, *96*, No. 041108.

(15) Tang, S.; Zhang, C.; Wong, D.; Pedramrazi, Z.; Tsai, H.-Z.; Jia, C.; Moritz, B.; Claassen, M.; Ryu, H.; Kahn, S.; Jiang, J.; Yan, H.; Hashimoto, M.; Lu, D.; Moore, R. G.; Hwang, C.-C.; Hwang, C.; Hussain, Z.; Chen, Y.; Ugeda, M. M.; Liu, Z.; Xie, X.; Devereaux, T. P.; Crommie, M. F.; Mo, S.-K.; Shen, Z.-X. Quantum spin Hall state in monolayer 1T'-WTe_2. *Nat. Phys.* **2017**, *13*, 683.

(16) Li, W.; Li, J. Ferroelasticity and domain physics in two-dimensional transition metal dichalcogenide monolayers. *Nat. Commun.* **2016**, *7*, 10843.

(17) Naylor, C. H.; Parkin, W. M.; Ping, J.; Gao, Z.; Zhou, Y. R.; Kim, Y.; Streller, F.; Carpick, R. W.; Rappe, A. M.; Drndić, M.; Kikkawa, J. M.; Johnson, A. T. C. Monolayer single-crystal 1T'-$MoTe_2$ grown by chemical vapor depositionexhibits weak antilocalization effect. *Nano Lett.* **2016**, *16*, 4297.

(18) Wang, G.-Y.; Xie, W.; Xu, D.; Ma, H.-Y.; Yang, H.; Lu, H.; Sun, H.-H.; Li, Y.-Y.; Jia, S.; Fu, L.; Zhang, S.; Jia, J.-F. Formation mechanism of twin domain boundary in 2D materials: The case for WTe_2. *Nano Res.* **2019**, *12*, 569.

(19) Tersoff, J.; Hamann, D. R. Theory of the scanning tunneling microscope. *Phys. Rev. B: Condens. Matter Mater. Phys.* **1985**, *31*, 805.

(20) Young, S. M.; Kane, C. L. Dirac semimetals in two dimensions. *Phys. Rev. Lett.* **2015**, *115*, 126803.

(21) Chhowalla, M.; Shin, H. S.; Eda, G.; Li, L.-J.; Loh, K. P.; Zhang, H. The chemistry of two-dimensional layered transition metal dichalcogenide nanosheets. *Nat. Chem.* **2013**, *5*, 263.

(22) Cho, S.; Kang, S. H.; Yu, H. S.; Kim, H. W.; Ko, W.; Hwang, S. W.; Han, W. H.; Choe, D.-H.; Jung, Y. H.; Chang, K. J.; Lee, Y. H.; Yang, H.; Kim, S. W. Te vacancy-driven superconductivity in orthorhombic molybdenum ditelluride. *2D Mater.* **2017**, *4*, No. 021030.

(23) Hohenberg, P.; Kohn, W. Inhomogeneous electron gas. *Phys. Rev.* **1964**, *136*, B864.

(24) Kohn, W.; Sham, L. J. Self-consistent equations including exchange and correlation effects. *Phys. Rev.* **1965**, *140*, A1133.

(25) Kresse, G.; Furthmüller, J. Efficient iterative schemes for ab initio total-energy calculations using a plane-wave basis set. *Phys. Rev. B: Condens. Matter Mater. Phys.* **1996**, *54*, 11169.

(26) Kresse, G.; Hafner, J. Ab initio molecular dynamics for liquid metals. *Phys. Rev. B: Condens. Matter Mater. Phys.* **1993**, *47*, 558.

(27) Blöchl, P. E. Projector augmented-wave method. *Phys. Rev. B: Condens. Matter Mater. Phys.* **1994**, *50*, 17953.

(28) Kresse, G.; Joubert, D. From ultrasoft pseudopotentials to the projector augmented-wave method. *Phys. Rev. B: Condens. Matter Mater. Phys.* **1999**, *59*, 1758.

(29) Perdew, J. P.; Burke, K.; Ernzerhof, M. Generalized gradient approximation made simple. *Phys. Rev. Lett.* **1996**, *77*, 3865.

(30) Artacho, E.; Sánchez-Portal, D.; Ordejón, P.; García, A.; Soler, J. M. Linear-scaling ab-initio calculations for large and complex systems. *Phys. Status Solidi B* **1999**, *215*, 809.

(31) Kim, H.-J.; Kang, S.-H.; Hamada, I.; Son, Y.-W. Origins of the structural phase transitions in $MoTe_2$ and WTe_2. *Phys. Rev. B: Condens. Matter Mater. Phys.* **2017**, *95*, 180101.

(32) Artacho, E.; Anglada, E.; Diéguez, O.; Gale, J. D.; García, A.; Junquera, J.; Martin, R. M.; Ordejón, P.; Pruneda, J. M.; Sánchez-Portal, D.; Soler, J. M. The SIESTA method; developments and applicability. *J. Phys.: Condens. Matter* **2008**, *20*, No. 064208.

(33) Sánchez-Portal, D.; Ordejón, P.; Artacho, E.; Soler, J. M. Density-functional method for very large systems with LCAO basis sets. *Int. J. Quantum Chem.* **1997**, *65*, 453.

(34) Troullier, N.; Martins, J. L. Efficient pseudopotentials for plane-wave calculations. *Phys. Rev. B: Condens. Matter Mater. Phys.* **1991**, *43*, 1993.

(35) Kleinman, L.; Bylander, D. M. Efficacious form for model pseudopotentials. *Phys. Rev. Lett.* **1982**, *48*, 1425.